ELSEVIER

Cavity-configuration-dependent instability in a tightly focused end-pumped solid-state laser

Ching-Hsu Chen *, Po-Tse Tai, Wen-Feng Hsieh *

*Department of Photonics and Institute of Electro-Optical Engineering, National Chiao Tung University, 1001 Tahsueh Rd.,
Hsinchu 30050, Taiwan*

Abstract

We experimentally studied the cavity-configuration-dependent instability in an end-pumped Nd:YVO$_4$ laser in the vicinity of the degenerate resonator configuration of $g_1g_2 = 1/4$ with small pump size. We found that the laser instability occurs in a narrow range of cavity tuning on each side of the degeneracy, which shows periodic, period-doubling, and chaotic time evolutions. By using Collin's integral together with rate equations and taking into account the thermal lens effect, we show that the simulation is consistent with the experiments. The observed instabilities are new and, as far as we know, this is the first report that discusses the relationship between the instability and the thermal lens effect.
© 2004 Elsevier B.V. All rights reserved.

PACS: 42.60.Mi; 42.60.Jf; 42.55.Xi

1. Introduction

It is commonly believed that spontaneous instabilities are impossible in class B lasers described by simple two-level rate equations without an additional degree of freedom such as external modulation, light injection, delayed feedback, etc. [1]. However, the transverse effects such as gain variation and diffraction in the resonator provide the additional degree of freedom and have been demonstrated to play important roles in lasers [2,3]. Because various transverse modes may be excited especially when the laser is operated at near-degeneracy, a degenerate resonator is thus a good choice for obtaining laser instabilities. Previously, we have analyzed an iterative map of the q-parameter of the resonator [4] and concluded that a laser will become unstable near some degenerate cavity configurations under non-linear effects. Using an end-pumped cw Nd:YVO$_4$ laser, we have studied different laser behaviors under various pump sizes

---
* Corresponding authors. Tel.: +886-65724805; fax: +886-35716631.
E-mail addresses: q1410928@ms38.hinet.net (C.-H. Chen), wfhsieh@mail.nctu.edu.tw (W.-F. Hsieh).

[5,6] when the cavity is near 1/3-transverse degeneracy ($g_1g_2 = 1/4$). Recently, the Petermann K factor has also been calculated for maxima on each side of the degeneracy under strong gain guiding or small pump size [7]. It was emphasized that in the vicinity of the degeneracies the empty-cavity degenerate transverse modes are phase-locked and the resultant radial phase profile depends strongly on the cavity-length detuning.

In this work, we study the cavity-configuration-dependent instability and determine the unstable regions with cavity length, pump power, and pump size as the control parameters. When the pump size is small, we found that the laser always exhibits a stable cw output, except for a narrow range of cavity tuning on each side of the degeneracy. The temporal behaviors of the laser output show periodic, period-doubling, and chaotic evolutions. We also observed various patterns in the far field when we scanned the cavity length. In particular, an anomalous mode pattern is accompanied with frequency beating close to the point of degeneration. The simulation by the use of Collin's integral and rate equations, while taking into account the thermal lens effect, shows good agreement with the experiment. The observed instabilities are new and, as far as we know, this is the first report that discusses the relationship between the instability and the thermal lens effect. We describe our experiments in Section 2 and then simply discuss the numerical model and show the numerical results in Section 3. The conclusions are presented in Section 4.

2. The experiments

The experimental setup is schematically shown in Fig. 1. This laser contains a 1-mm thick Nd:YVO4 laser crystal whose one end face acted as an end mirror and a spherical mirror with radius of curvature of 8 cm as the output coupler (OC). A cw near-TEM$_{00}$ Ti–sapphire laser at wavelength of 808 nm was used as the pump source, which was focused by a collimating lens onto the crystal so the pump size was adjustable. The end face of the crystal, which acted as the end mirror and faced the pump beam, had a dichroic coating with
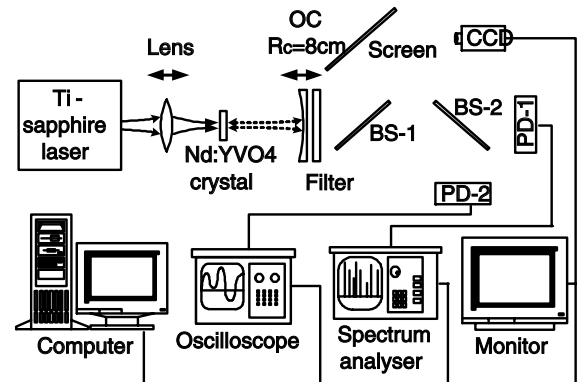

Fig. 1. The schematic experimental set up. BS is the beam splitter.

greater than 99.8% reflection at 1.064 μm and greater than 99.5% transmission at 808 nm; the other end face comprised an antireflection layer at 1.064 μm to avoid the effect of intracavity etalons. The OC of 10% transmission was mounted upon a translation stage so we could tune the cavity length (L) near the degenerate configuration. The degeneration point of $g_1g_2 = 1/4$, which corresponds to $L = 6$ cm, was determined by the cavity length where the lowest lasing threshold occurs [8]. The laser output was split into two beams, one of which was recorded by a CCD camera and the other was further split into two beams that were individually collected by two photodiodes (PDs) with rise times < 0.3 ns. The signals of the PDs were then fed into a LECROY-9450A oscilloscope (bandwidth 200 MHz) and an HP8560E rf spectrum analyzer (bandwidth 2.9 GHz), respectively. The Gaussian pump radius, w_p, was determined by the standard knife method.

The output power varied with the cavity length under various pump radii and is shown in Fig. 2(a). The bottom three curves for $w_p = 19$ μm show that a higher pump power not only widens but also heightens the power hump. The laser exhibits a stable cw output for almost entire range of the studied 3-mm cavity tuning. However, within a narrow range of L on each side of the power hump, denoted as stars in Fig. 2(a), we always observed spontaneous instabilities. The top two curves are the cavity-length-dependent output power for $w_p = 25$ and 34 μm at a pump power of
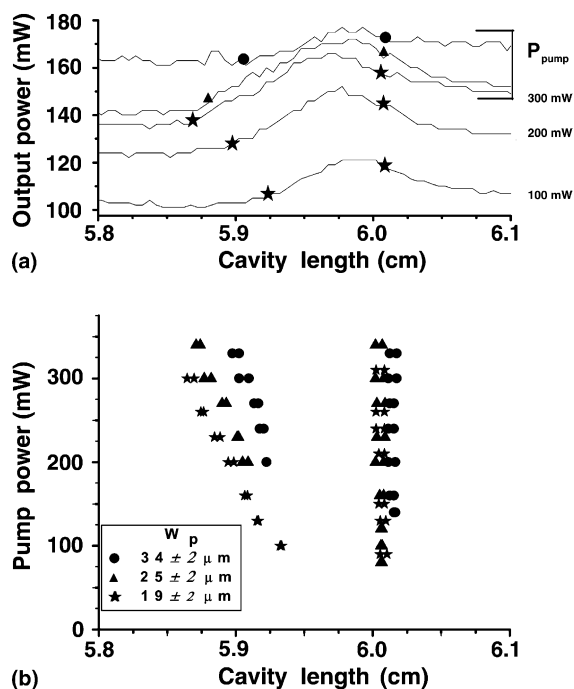
(a)

(b)

Fig. 2. The observed output power as a function of cavity length (a) and the unstable regions in terms of the cavity length and the pump power for different w_p (b). The symbols for w_p are the same in (a) and (b). The output power is around 40 mW for $P_{pump} = 100$ mW as $w_p = 19$ μm. Note that we have added 50 mW and 75 mW for the curves of $P_{pump} = 200$ mW and $P_{pump} = 100$ mW. The absorption efficiency of P_{pump} is about 60–70%. The lasing threshold is about 5–30 mW depending on L and w_p.

300 mW, in which the triangles and the solid circles denote the unstable regions for both cases. Note that the radius of cold-cavity fundamental mode is approximately 108 μm. Summarized in Fig. 2(b) are the unstable regions in terms of the cavity length and the pump power for the three pump sizes of 19, 25, and 34 μm. We use a single symbol to denote a narrow unstable region while twin symbols are used to encompass a wider unstable region of about 100 μm. One can see that the unstable regions on the short-cavity side are well separated for different w_p and located farther away from degeneracy with increasing the pump power; in contrast, those on the long-cavity side are located very close to the point of degeneration and are nearly independent of the pump power.

When the cavity length was tuned from the long-cavity side, toward and across the point of degeneration, various far-field mode patterns were observed. The mode pattern shows a near-fundamental Gaussian distribution far from degeneracy. Tuning L close to the right edge of the unstable region, we observed a slightly distorted mode pattern. When the cavity was set within about 100 μm of the unstable region, the mode pattern became non-cylindrically symmetric and strongly spread in a special direction as shown in Fig. 3(a). This anomalous spreading pattern maintained wider than the whole unstable region by few tens of micrometers. When L was tuned across the range that showed the spreading pattern, the far-field pattern recovered to a cylindrically symmetric one but turned into many concentric rings with a dark center that is the far-field pattern of the multi-beam-waist mode [6]. By further tuning of L toward the unstable region on the short-cavity side, we observed the cylindrically symmetric mode pattern as shown in Fig. 3(b) that differs from the patterns in the unstable region of the long-cavity side, as indicated in Fig. 3(a).

We further investigated the temporal behaviors of the output power within the unstable regions at $P_{pump} = 260$ mW and $w_p = 34$ μm. Fig. 4(a) shows a periodic time trace when the cavity was tuned at the edge of the long-cavity unstable region. Its corresponding rf spectrum in Fig. 4(b) shows one main peak at 1.33 MHz and three harmonics. When the cavity length was decreased by ∼20 μm from the position of Fig. 4(a), a period-2 evolution was observed. The time trace and its
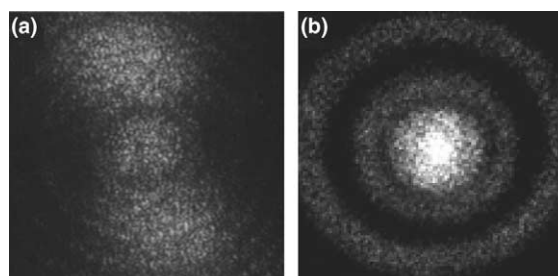

Fig. 3. The far-field mode patterns inside the long-cavity unstable region (a) and inside the short-cavity unstable region (b).
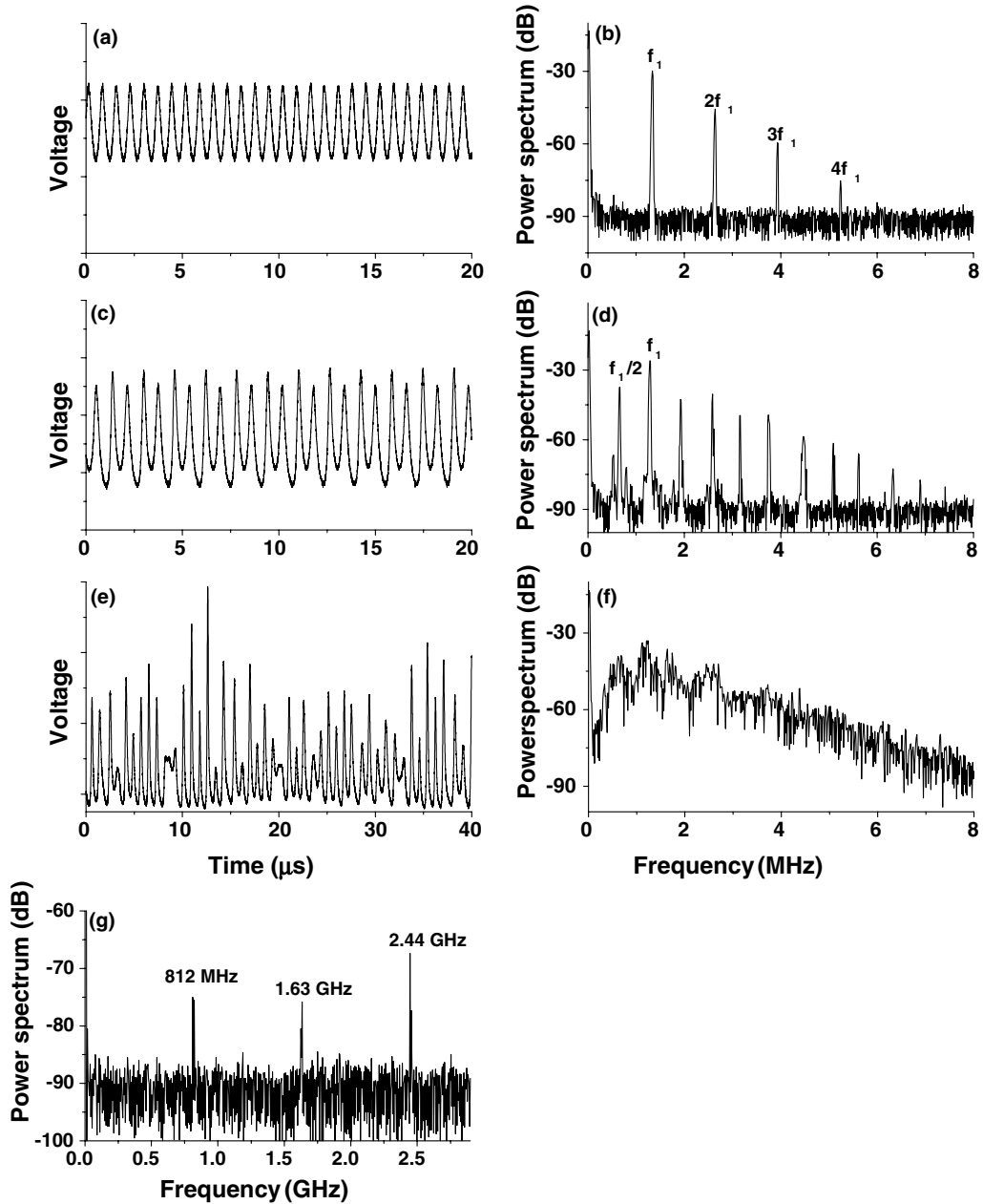
Fig. 4. The temporal evolution of laser output. (a) Periodic, (c) period-doubling, and (e) chaotic output within the long-cavity unstable region. The RF spectra (b), (d), and (f), that correspond to (a), (c), and (e), respectively. (g) The high frequency rf spectrum of the spreading mode pattern of Fig. 3(a).

spectrum are shown in Fig. 4(c) and (d), respectively. On continuing the decreasing of the cavity length, we recorded a chaotic evolution in Fig.

4(e) with a broad low frequency spectrum indicated in Fig. 4(f). Calculation by use of the chaos data analyzer (American Institute of Physics)

shows that the correlation dimension of the chaotic evolution is approximately 2.1.

Although the temporal behaviors of the cavity-configuration-dependent instabilities are similar on each side of the degeneracy, the high-frequency responses of their power spectra are quite different. For the long-cavity instabilities we observed multiple beating frequencies at 812 MHz, 1.63 GHz, and 2.44 GHz (see Fig. 4(g)) that were confirmed with a Fabry–Perot interferometer (FPI) having FSR = 15 GHz and finesse = 150. The transverse mode beating pertaining to the Laguerre–Gaussian $LG_{1,0}$ and/or $LG_{2,0}$ modes would induce spatiotemporal instability, where the subscripts 1 and 2 are the radial indices and 0 is the azimuthal index. However, within the short-cavity unstable region the spectrum shows only the longitudinal mode beating at 2.44 GHz with the absence of transverse mode beating in both of the rf and the FPI spectra.

To investigate the distinction between the instabilities on the long-cavity side and those of the short-cavity side, we used two PDs at different transverse positions to simultaneously record the laser power. The first PD was fixed at the center of the profile as reference and the second one was located at an off-axis position. When the two detectors were separated within a distance, their temporal traces on the oscilloscope were completely the same as shown in Fig. 5(a). However, we found for the long-cavity instability that the high peak of one trace coincided with the low peak of the other trace as shown in Fig. 5(b) when the two detectors were separated by some specific distance. This reveals that the intensity profile varies with time and thus indicates spatiotemporal instability. On the other hand, within the short-cavity unstable region, we always observed the same behavior between the two signals no matter at what position the second PD was located. Temporal instability was exhibited on the short-cavity side. In addition, we also found that the instabilities on both sides of the degeneracy are closely related to high-order transverse modes because the instabilities disappeared when a knife-edge was inserted ~500 μm into the cavity beam to inhibit the high-order transverse modes. This will be explained in the following section.
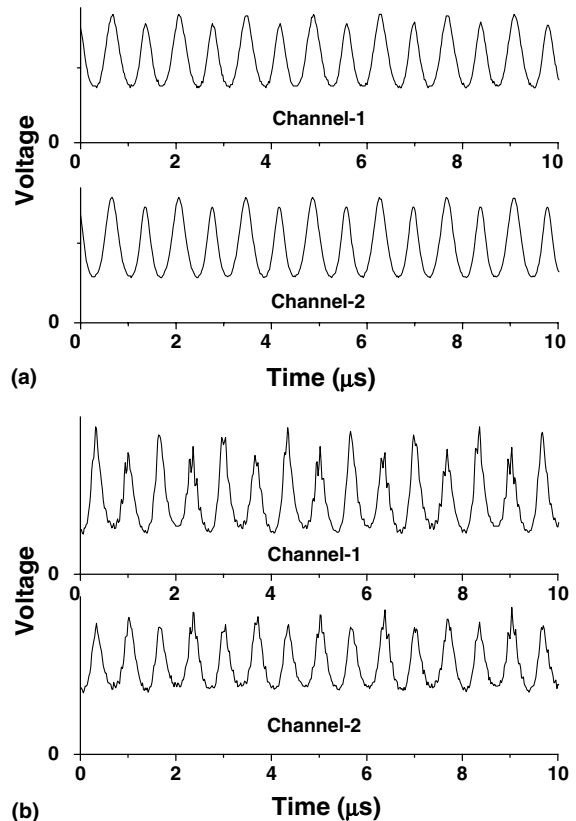

Fig. 5. The time traces in oscilloscope when the two PDs were separated close to each other (a) and farther away (b) for the long-cavity instabilities.

3. The simulations

In order to understand the cavity-dependent instability, we numerically simulated this laser system by using Collin's integral [9] together with the rate equations as described in our previous work [6]. The method was used to model a single-longitudinal multitransversal solid-state ring laser [10] and to analyze the decay rates of standing-wave laser cavities [11]. In our system the cylindrically symmetric resonator and the thin slab gain medium were assumed. We did not consider the dispersion of the active medium or frequency detuning between the atomic transition and the cavity mode, so the gain was assumed to be real. Given an initial gain distribution and an electric field, the field evolution will converge to a stationary solution if the

final state is a stable cw mode. In contrast, if the final state is unstable, the electric field will automatically evolve to a dynamical state. When the thermal lens effect was considered, we imposed a radial phase distribution in the diffraction integral from Eqs. (2), (6) and (11) of [12]. Thermal induced stress, thermal deformation of the crystal, and thermal fluctuation were neglected. To obtain the time evolution of the output power, we set the reference plane with a 600 μm aperture at the flat end mirror and laterally integrated the intensity profile for each round trip. The parameters that were used are the stimulated emission cross section of 25×10^{-19} cm^2, the spontaneous decay rate of 2×10^4 s^{-1}, the saturation parameter of the active medium of 1.12×10^{10} J F^{-1} m^{-2}, the fractional thermal loading of 0.23, the absorption coefficient of the laser crystal of 1930 m^{-1}, the thermal conductivity of 5.23 W m^{-1} K^{-1}, the thermal-optic coefficient of 8.5×10^{-6} K^{-1}, and the others are the same as described in Section 2.

Fig. 6(a) shows the output power as a function of L when considering the thermal lens effect. The curves of output power that are labeled as triangles, empty squares, and solid circles for $w_p = 25$, 30, and 35 μm, respectively, show asymmetric power humps with respect to the point of degeneration. The dependence of the power hump on w_p and P_p (the effective pump power) are the same as in Fig. 2(a). The unstable regions are summarized for four values of w_p in Fig. 6(b), which are similar to those in Fig. 2(b) except that the vertical axis of Fig. 6 is the effective pump power that matches with the pump efficiency of ∼0.6 taken from the measured pumping. Again, in Fig. 6(b) we use a single symbol to denote a narrow unstable region while twin symbols are used to encompass a wider unstable region. It shows similar unstable regions and dependence on w_p and P_p as those in Fig. 2(b); for example, at $w_p = 35$ μm, the unstable region shifts approximately from $L = 5.94$ to 5.90 cm on the short-cavity side as one increases the effective pump power to match with the experiment data in Fig. 2(b). Moreover, the far-field intensity profiles beside the long-cavity unstable region are similar to those in Fig. 2(b) of [6]. In addition, no instability can be observed as $w_p > 40$ μm, which is also consistent with the experiment.
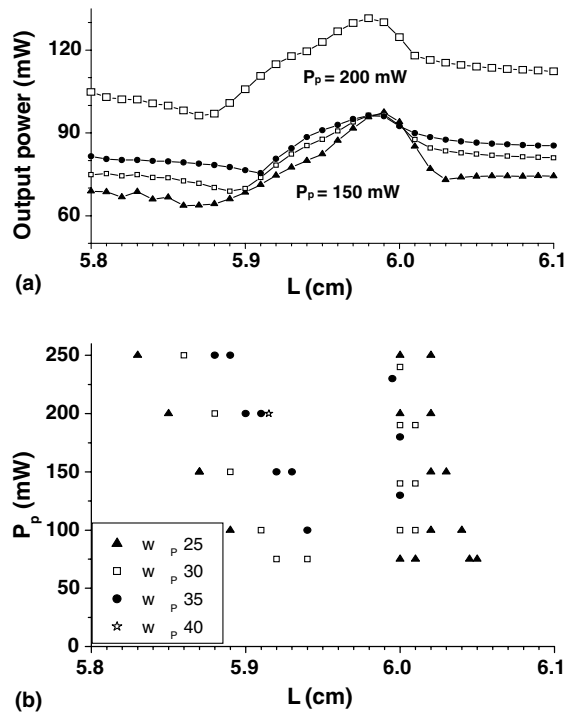

Fig. 6. The numerical output power as a function of cavity length with considering the thermal lens effect (a) and the unstable regions (b) for different w_p. The symbols for w_p are the same for (a) and (b).

To study the influence of the thermal lens effect, we repeated the simulation without considering the thermal lens effect. The calculated output power and the obtained unstable regions are shown in Fig. 7(a) and (b), respectively. As compared with Fig. 6, we found the thermal lens effect leads to certain phenomena: (1) an asymmetrical shape of the power hump; (2) asymmetrical unstable regions with respect to the degeneration point; (3) dependence of the region shift on P_p on the short-cavity side but not on the long-cavity side; and (4) much less shift of the power maximum than shift of the unstable region (e.g., see $w_p = 30$ μm and $P_p = 150$ mW).

Without the thermal lens effect, not only the power hump but also the dynamical behaviors are symmetric with respect to the point of degeneration. The simulated temporal evolution of the unstable output power exhibits self-pulsation on both sides of the degeneracy with a pulsing frequency of
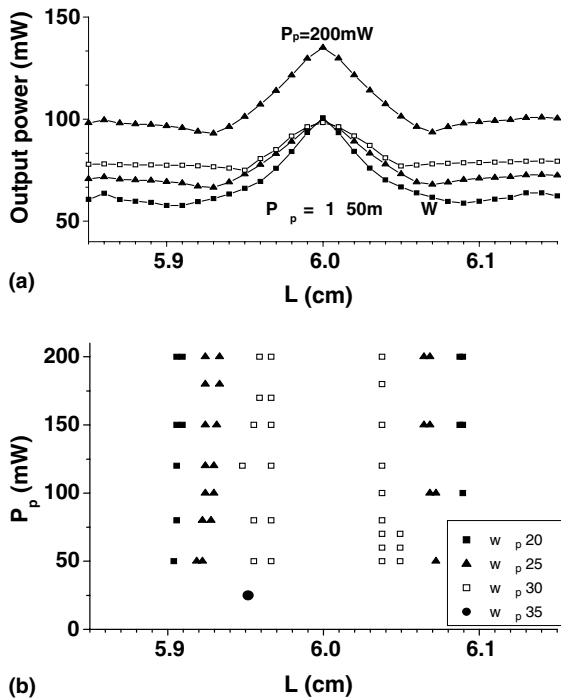
Fig. 7. The numerical output power as a function of cavity length (a) and the unstable regions (b) without considering the thermal lens effect. The symbols for w_p are the same for (a) and (b).

few hundred kHz (see Fig. 8(a)). The simulated intensity profile of each round trip show the variation of the on-axis peak intensity with time as the characteristic feature of Fig. 8(a), but the normalized profile varies only a little. We plotted four normalized intensity profiles in Fig. 8(b) from the pulse peak to valley to show the variation. Their corresponding far-field intensity profiles [insets in Fig. 8(b)], having two obvious rings, agree with the photograph of Fig. 3(b). Moreover, the far-field intensity profile decreases smoothly and then increases when the pulse is growing. This leads to pure temporal instability. The modal analysis shows that the modes in Fig. 8(b) can be decomposed into the combination of the near-degenerate $LG_{0,0}, LG_{3,0}, \ldots, LG_{18,0}$ modes with mode weights and relative phase shifts because $LG_{21,0}$ undergoes large diffraction losses for a 600 μm aperture at the reference plane. These phase shifts must be included because the phase pattern is important as

emphasized in [7]. We give a fitted result in the figure caption of Fig. 8(b). When the thermal lens effect is included, the feature of self-pulsation is unchanged for the short-cavity side. This matches with the general expectation that the thermal lens effect will only shift the cavity length.

However, on the long-cavity side the region shift seems independent of P_p and the self-pulsation becomes the characteristic feature of Fig. 8(c), in which the output power forms three branches of oscillation. The first 20 iterations in the inset show that the output evolution nearly comes back the same value after three round trips; that is the power spectrum indicates one peak at roughly 1/3-longitudinal beating frequency that corresponds to the experimental data of 812 MHz. The intensity profiles of three successive round trips are shown in Fig. 8(d), which are not normalized due to the large difference. The corresponding far-field intensity profiles in the inset of Fig. 8(d) exhibit a complex feature, which is different from that of the short-cavity side. Unfortunately, we could not yet obtain good fitting data by running the same fitting parameters, even when the $LG_{1,0}$ mode was included. This may be due to the peculiar phase pattern that is deformed strongly by the thermal lens effect in the vicinity of the degeneracy. Because the beating frequency between the near-degenerate LG modes are absent on both long-cavity and short-cavity instabilities, the frequencies of the near-degenerate LG modes are locked together to a single frequency. Therefore the frequency-locked mode, a supermode [13], interacts with the inverted populations and thus leads to the short-cavity instabilities. However, the long-cavity instabilities arise mainly from the frequency beating between the supermode and the other empty-cavity modes. Although the asymmetric (spreading) mode pattern of Fig. 3(a) cannot be produced by using the cylindrically symmetric model with single optical frequency, the simulated results agree with the experiment of transverse mode beating. As far as we know, this is the first report that discusses the relationship between the instability and the thermal lens effect.

Furthermore, when the aperture on the reference plane is decreased to 450 μm, in accordance
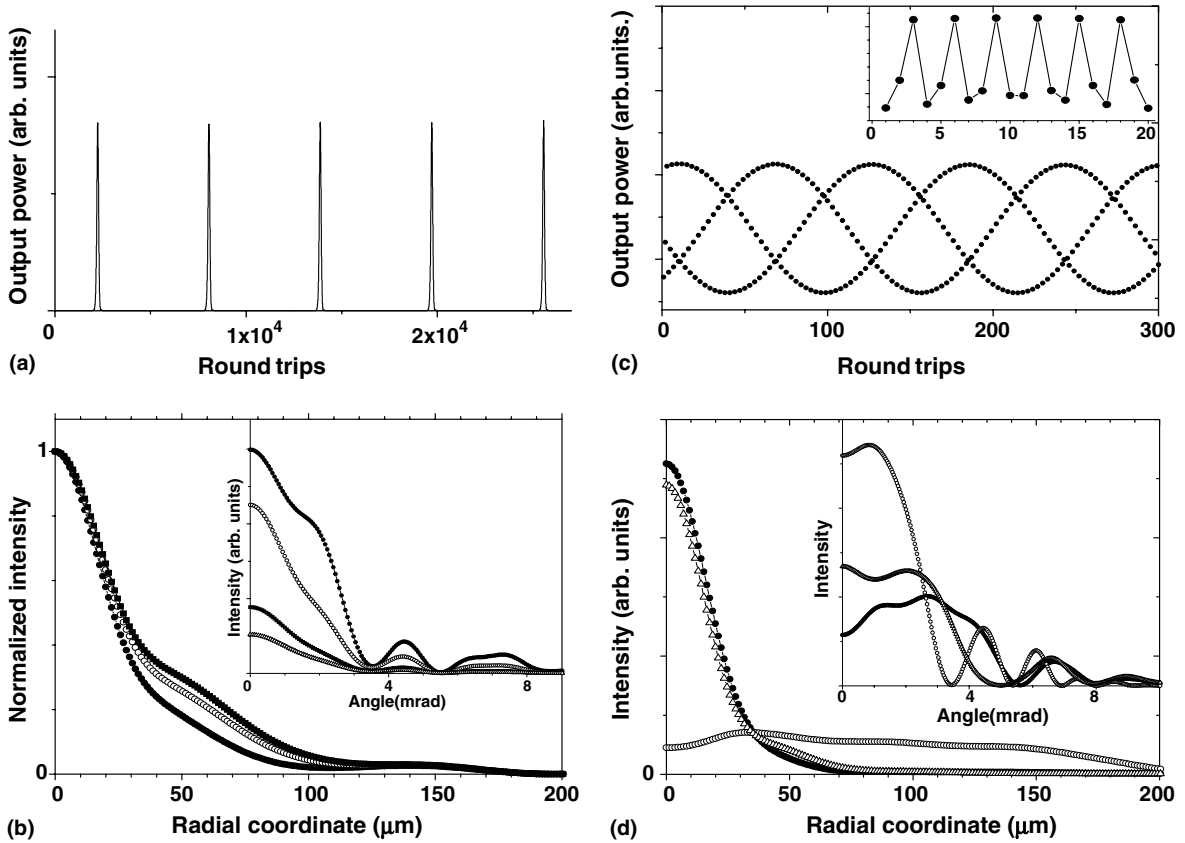
Fig. 8. (a) A self-pulsing temporal evolution of the simulated output power without the thermal lens effect for $L = 5.96$ cm. (b) The normalized intensity profiles and their corresponding far-field profiles (inset) from the pulse peak (solid circles) changes to open circles, solid squares and then to the pulse valley (open triangles). The normalized profiles of the open triangles are covered by the solid squares. The modal analysis for the profile of solid squares are $LG_{0,0}(0°) + 0.63\ LG_{3,0}(-75°) + 0.34\ LG_{6,0}(-105°) + 0.16\ LG_{9,0}(-90°) + 0.08\ LG_{12,0}(-83°) + 0.08\ LG_{15,0}(-116°) + 0.07\ LG_{18,0}(-93°)$. (c) The numerical temporal evolution of the output power in the vicinity of the degeneracy with the thermal lens effect for $L = 6.005$ cm. Inset is the first 20 iterations. (d) The intensity profiles and their corresponding far-field profiles (inset) of three successive round trips.

with the experiment described in Section 2, the instability disappears. The stationary mode now consists of the near-degenerate LG modes with the same frequency but lack of the higher-order $LG_{15,0}$ and $LG_{18,0}$ modes. This fact of transverse mode locking was confirmed by the absence of the near-degenerate mode beating and by the observation of the intensity profile variation with the propagation distance as done in [6]. The supermode lack of the components of the $LG_{15,0}$ and $LG_{18,0}$ modes is unable to arise the instability. Inserting a knife-edge into the cavity beam in our experiment also results in a cylindrically symmetric

pattern instead of a spreading pattern. Apparently, the high-order modes with small amplitude may play important roles in symmetry breaking as indicated in [14]. However, the origin of the symmetry breaking is still unknown.

Going back to Fig. 8(a), the pulsation is damped by the relaxation oscillation so the pulsing frequency depends on the pump power and the cavity length. Theoretically, the pulsing spectrum can be calculated from the Fourier transform of the output power evolution. Interestingly, by using $\gamma = 1 \times 10^5$ s^1 we obtained periodic pulsing, period-2, and chaotic time evolution of the output power

when L was tuned from 5.96 to 5.951 cm with $w_p = 30$ μm and an effective pump power of 100 mW. For $L = 5.948$ cm a homoclinic orbit was clearly seen in the phase portrait reconstructed from the standard time-delay technique. The routes to chaos both through Hopf bifurcation and through intermittency associated with the homoclinic orbit were shown in an end-pumped standing-wave alexandrite laser [15]. It is possible that our laser performs homoclinic dynamics because our simulation is consistent with the experiment but this may be further studied and discussed elsewhere.

4. Conclusions

We have found the cavity-configuration-dependent instabilities and determined the two sets of the unstable regions beside the degeneracy near $g_1 g_2 = 1/4$ in an end-pumped Nd:YVO$_4$ laser with small pump sizes. We illustrated the temporal behavior of the instabilities including the chaotic output. The different far-field patterns beside the unstable regions were observed; in particular, a special spreading mode pattern was observed in the vicinity of the degeneracy. Our numerical results, which were obtained using a cylindrically symmetric model with single frequency, agree well with the experiments and reveal the influence of the thermal lens effect.

References

[1] C.O. Weiss, R. Vilaseca, Dynamics of Lasers, VCH, New York, 1991.
[2] L.A. Lugiato, F. Prati, L.M. Narducci, P. Ru, J.R. Tredicce, D.K. Bandy, Phys. Rev. A 37 (1988) 3847.
[3] L.A. Lugiato, G.L. Oppo, J.R. Tredicce, L.M. Narducci, M.A. Pernigo, J. Opt. Soc. Am. B 7 (1990) 1019.
[4] M.D. Wei, W.F. Hsieh, C.C. Sung, Opt. Commun. 146 (1998) 201.
[5] C.H. Chen, M.D. Wei, W.F. Hsieh, J. Opt. Soc. Am. B 18 (2001) 1076.
[6] C.H. Chen, P.T. Tai, M.D. Wei, W.F. Hsieh, J. Opt. Soc. Am. B 20 (2003) 1220.
[7] C.F. Maes, E.M. Wright, Opt. Lett. 29 (2004) 229.
[8] H.H. Wu, W.F. Hsieh, J. Opt. Soc. Am. B 18 (2001) 7.
[9] S.A. Collins, J. Opt. Soc. Am. 60 (1970) 1168.
[10] F. Hollinger, Chr. Jung, J. Opt. Soc. Am. B 2 (1985) 218.
[11] Y.J. Cheng, P.L. Mussche, A.E. Siegman, IEEE J. Quantum Electron. 31 (1995) 391.
[12] M.E. Innocenzi, H.T. Yura, C.L. Fincher, R.A. Field, Appl. Phys. Lett. 56 (1990) 1831.
[13] H. Lin, N.B. Abraham, Opt. Commun. 79 (1990) 476.
[14] E.J. D'Angelo, C. Green, J.R. Tredicce, N.B. Abraham, S. Balle, Z. Chen, G.L. Oppo, Physica D 61 (1992) 6.
[15] W. Gadomski, B. Ratajska-Gadomska, J. Opt. Soc. Am. B 17 (2000) 188.